J. Mazurenko[1,2], L. Kaykan[3], Kh Bandura[1], O. Vyshnevskyi[4], M. Moiseienko[1],
M. Kuzyshyn[1], N. Ostapovych[1]

Analysis of the Structural, Morphological, and Elastic Properties of Nanosized CuFe₂O₄ Spinel Synthesized via Sol-Gel Self-Combustion Method

[1]Ivano-Frankivsk National Medical University, Ivano-Frankivsk, Ukraine, yumazurenko@ifnmu.edu.ua;
[2]Faculty of Physics and Applied Computer Science, AGH University of Krakow, Krakow, Poland;
[3]G.V. Kurdyumov Institute for Metal Physics, N.A.S. of Ukraine, larysa.kaykan@gmail.com;
[4]Department of Diamond, M.P. Semenenko Institute of Geochemistry, Mineralogy, and Ore Formation NAS of Ukraine, Kyiv, Ukraine, vyshnevskyy@i.ua

Nanosized CuFe₂O₄ ferrite was synthesized through the sol-gel self-combustion technique, using iron and copper nitrates with citric acid as fuel. The synthesized ferrite was subsequently analyzed using X-ray diffraction (XRD), Fourier transform infrared spectroscopy (FTIR), and Scanning Electron Microscopy (SEM). X-ray diffraction studies validated the crystalline nature of the CuFe₂O₄, identifying it as having a mixed spinel structure within the Fd3m space group. Particle sizes were quantified using several methods including Debye-Scherrer, Williamson-Hall, Halder-Wagner, modified Debye-Scherrer, and size-strain plot (SSP), with all methods indicating a consistent average particle size of 28 nm. The elastic properties of the nanoparticles were extensively characterized, utilizing both diffraction line broadening (via the Williamson-Hall method) and Fourier-transform infrared spectroscopy (FTIR) to evaluate the materials' structural dynamics. Additionally, microstrain within the crystal lattice and various elastic constants, such as Young's modulus, Shear modulus, Debye temperature, and the velocities of longitudinal and transverse wave propagation were calculated. An electron density distribution was also constructed from the X-ray diffraction data, providing insight into the electronic environment and bonding characteristics of the material.

Keywords: Nanostructured materials; Copper Ferrite; Sol-Gel Self-Combustion; X-ray diffraction; Microstructural analysis; Halder-Wagner method; Scanning electron microscopy.

Introduction

Nanosized ferrites, with dimensions under 100 nm, gather significant interest for their distinctive physicochemical properties [1, 2] that develop from the enhanced surface activity compared to their bulk forms. The size of these particles critically influences their elastic [3], magnetic [4], optical [5], and degradation characteristics [6]. The shape and size of the nanoparticles vary based on the synthesis conditions and methods used [7, 8]. This variability underscores the importance of accurately determining the particle sizes. Owing to their small size and unique properties, nanosized ferrites find extensive applications across various scientific domains, including microwave technology [9], gas sensing [10], catalysis in hydrogen production [11], and the degradation and elimination of organic pollutants [12], phenols [13], and antibiotics [14].

Recently, ferrite nanoparticles have gained attention in the medical and biological fields [15] due to their magnetic properties. They are being extensively researched for various applications, including serving as contrast agents in magnetic resonance imaging [16], enabling targeted drug delivery within the body [17], and

aiding in the diagnosis and treatment of cancer, including the use of hyperthermia [18]. Additionally, their bactericidal properties are being explored for combating a wide range of pathogens [19, 20].

Within the broad spectrum of magnetic nanomaterials, ferrite spinel CuFe$_2$O$_4$ is notably outstanding for its extensive research and practical applications. This compound can crystalize either a cubic structure, of the space group Fd3m [21], or a tetragonal structure, identified by the space group I41/amd [22]. The specific structural form of CuFe$_2$O$_4$ is influenced by factors such as the synthesis method [23], post-synthesis annealing temperatures [24], and dopant substitution [25]. Both cubic and tetragonal forms of CuFe$_2$O$_4$ can be synthesized through various appropriate techniques. In these nanocrystals, internal deformation occurs due to surface effects, which arise from size constraints. These elastic properties can be modified by adjusting synthesis parameters, including pH, the type and quantity of substituting material, and annealing conditions [26].

In nanocrystals, the inherent size constraints lead to internal deformations, resulting in the broadening of diffraction peaks observed in diffractograms. This peak broadening is attributed to two factors: the size of the particles and deformation within the crystal lattice [27]. Common sources of lattice deformation include dislocation density, point defects, grain boundaries, packing defects, and sintering defects [28]. Therefore, by analyzing the extent of diffraction peak broadening, it is possible to indirectly assess the size of the coherent scattering regions (CSR), quantify the internal strain, and estimate the energy density of the elastic strain. To analyze these effects, several methods are employed, including Williamson-Hall [29], Warren-Averbach [30], and Balzar [31]. The Warren-Averbach and Balzar methods use Fourier-Stokes decomposition to dissect the components, whereas the Williamson-Hall method, known for its simplicity, utilizes the half-width of diffraction peaks to determine various elastic properties, including microstresses, and to estimate average particle sizes.

In this study, the elastic properties of CuFe$_2$O$_4$ nanoferrites synthesized via the sol-gel autocombustion method were characterized using XRD data. This included Williamson-Hall analysis, the size-strain plot (SSP), and the Halder-Wagner method, which helped establish the average particle sizes. Additionally, the elastic characteristics of the synthesized spinels were further analyzed through Fourier-transform infrared spectroscopy (FTIR) data, and electron density maps derived from the XRD data also provided insights into the material's structure.

I. Materials and Methods

1.1. Synthesis

CuFe$_2$O$_4$ samples were synthesized using the sol-gel autocombustion method [32-34]. The initial reagents, which included copper nitrate [Cu(NO$_3$)$_3$·3H$_2$O], iron nitrate [Fe(NO$_3$)$_3$·9H$_2$O], and citric acid [C$_6$H$_8$O$_7$], were purchased from LobaChemie, India. These materials were measured in stoichiometric proportions and dissolved in distilled water. The solutions were thoroughly mixed

using a magnetic stirrer to ensure a homogeneous mixture. Following this, a citric acid solution was introduced in a 1:1.25 ratio to the metal content and mixed vigorously. To adjust the pH to 7, an aqueous ammonia solution was added. The mixture was then maintained at 350 K to evaporate excess water, forming a viscous gel that eventually dried into a xerogel. This xerogel was subsequently heated to 450 K in an oven where it ignited and transformed into a lightweight, cellular dendritic structure. This structure was then ground into a fine powder for further analysis.

1.2. XRD and SEM Studies

The structural and phase composition of the samples were analyzed using an Empyrean PANalytical X'Pert Pro powder diffractometer, equipped with a Bragg–Brentano configuration, a Cu Long Fine Focus X-ray tube (Kα line λ = 1.54051 Å), a Ni filter to suppress Kβ radiation, and a curved graphite monochromator. X-ray diffraction scans covered 2θ angles from 10° to 70°, with a step size of 0.033° and an acquisition time of 50 seconds per step to facilitate temperature assessments.

Data from these analyses were interpreted and used to compute structural and morphological parameters through the FullProf software, using Rietveld refinement techniques. Additionally, particle sizes were determined using a JSM-6700F electron microscope, operating in SEI mode at 10.0kV, with a magnification of x100,000 and a working distance of 6.4 mm to capture images at a resolution of 100 nm.

1.3. FTIR Analysis

Infrared absorption measurements were conducted using a Bruker VERTEX 70v Fourier transform infrared spectrometer, operating at a resolution of 2 cm^{-1}. The FT-FIR spectra were obtained on polyethylene windows from powdered samples that were mixed with Apiezon grease.

II. Results and Discussion

2.1. Xray diffraction studies

Figure 1 displays the X-ray diffraction pattern of copper ferrite synthesized using the sol-gel self-combustion method. The diffraction peaks observed at 2θ angles of 30.3, 35.7, 37.3, 43.3, 53.7, 57.3, and 62.9 correspond to the crystallographic planes (220), (311), (222), (400), (422), (333), and (440) respectively. These planes are in agreement with the Joint Committee on Powder Diffraction Standards (JCPDS) card number 25-0283 [35].

In addition to the predominantly cubic spinel phase (91.3%), a minor presence (8.7%) of the CuFeO$_2$ phase is also observed (JCPDS 39-0246). This secondary phase likely formed due to a slight deficiency in citric acid, which prevented the reaction from reaching the higher temperatures necessary for exclusive single-phase spinel formation. Given the dominance of the cubic spinel content, the impact of the secondary phase on the overall structural formations is considered negligible.
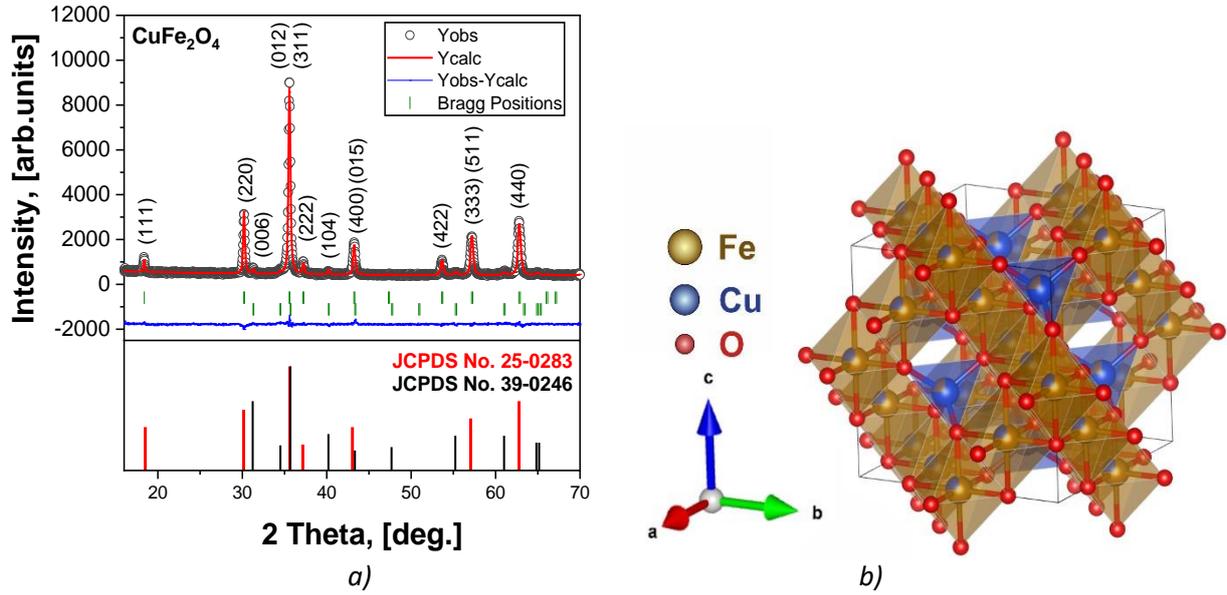
Fig. 1. (a) The X-ray patterns of CuFe₂O₄ synthesized via the sol-gel autocombustion method. The experimental data was refined using the Rietveld method. (b) Cubic crystal structure produced by VESTA-ver.3.5.8 [36].

2.1.1. Scherrer's method

In nanocrystals, X-ray diffraction peak broadening is influenced by the crystal size effect and internal strain, leading to two main types of broadening: physical and instrumental broadening [37]. Instrumental broadening can be adjusted using the following formula:

$$\beta_d^2 = \beta_m^2 - \beta_i^2 \qquad (1)$$

Where β_m represents the measured broadening, β_i is the instrumental broadening, and β_d is the broadening corrected for instrumental effects. Crystalline silicon was employed as a standard reference material for calibrating position and calculating instrumental broadening. Both instrumental and physical broadening of the sample were quantified as the full width at half maximum (FWHM).

With the physically corrected broadening, the average particle size is determined using the Scherrer equation [38]:

$$D = \frac{0.9\lambda}{\beta_d} \frac{1}{cos\theta} \qquad (2)$$

Where λ represents the wavelength of the incident radiation, and D is the average particle size. From our calculations, D is found to be 28.43 nm. This can be reformulated as:

$$cos\theta = \frac{0.9\lambda}{\beta_d} \frac{1}{D} \qquad (3)$$

By plotting $1/\beta_d$ against $cos\theta$ for CuFe₂O₄ nanoparticles, as illustrated in Fig. 2, known as the Scherrer plot, we derive the average particle size directly from the slope of the plot, which confirms it to be 28.43 nm.
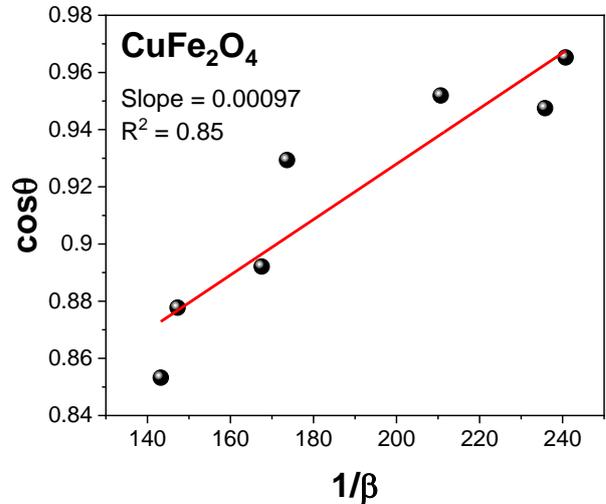
Fig. 2. Scherrer plot for CuFe₂O₄ nanoparticles.

2.1.2. Williamson-Hall analysis

Scherrer's formula primarily accounts for the influence of crystallite size on X-ray diffraction (XRD) patterns, but it does not address the microstructural aspects of the crystal lattice, such as internal deformations that arise in nanocrystals due to point defects, grain boundaries, triple junctions, and stacking defects [39]. Various methods, including the Williamson-Hall method and the Warren-Averbach method, consider the effects of strain-induced peak broadening in XRD and provide means to calculate both intrinsic strain and particle size. The Williamson-Hall (W-H) method is particularly noted for its simplicity and efficiency [40]. This method posits that the physical broadening of the X-ray diffraction peak is a function of both the size and microstrain within the nanocrystals, allowing for an integrated analysis of overall peak broadening.

According to this approach, the physical broadening of the X-ray diffraction peak is influenced by the size and microstrain of the nanocrystals, allowing the overall peak broadening to be expressed as [40]:

$$\beta_{total} = \beta_{size} + \beta_{strain} \qquad (4)$$

In the Williamson-Hall formula, it is assumed that the deformation is uniform along the entire crystallographic direction, that is, the deformation is isotropic and can be expressed as

$$\beta_{deformation} = 4\varepsilon tan\theta \qquad (5)$$

Thus, the total broadening due to strain and size at a particular peak having a value of hkl can be expressed as

$$\beta_{hkl} = \beta_{size} + \beta_{strain} \qquad (6)$$

Where, β_{hkl} is the full width at half maximum intensity for different diffraction planes.

$$\beta_{hkl} = \frac{k\lambda}{D} \cdot \frac{1}{cos\theta} + 4\varepsilon tan\theta \qquad (7)$$

From equation (7), by rearranging the terms, we obtain:

$$\beta_{hkl} \cdot cos\theta = \frac{k\lambda}{D} \cdot + 4\varepsilon sin\theta \qquad (8)$$

Equation (8) represents a linear relationship that considers the isotropic nature of crystals. Figure 3 displays a plot of this equation, where the term ($4sin\theta$) is plotted on the X-axis and ($\beta_{hkl} \cdot cos\theta$) on the Y-axis for each diffraction peak of CuFe$_2$O$_4$ nanoparticles. The slope of this line indicates the level of internal deformation, and the Y-intercept provides the average particle size of the CuFe$_2$O$_4$ nanocrystals. Lattice deformations in nanocrystals primarily arise from lattice expansion or contraction due to size constraints, as the atomic arrangement is slightly altered compared to their bulk counterparts. Additionally, size limitations often lead to the formation of many defects within the crystal lattice, further contributing to lattice deformation. The average particle size, estimated using the uniform strain model, was approximately 28 nm. Moreover, the positive slope of the Uniform Deformation Model (UDM) diagram suggests lattice expansion [41], indicative of intrinsic deformation within the nanocrystals. From this slope, the internal strain was calculated to be 0.00199.
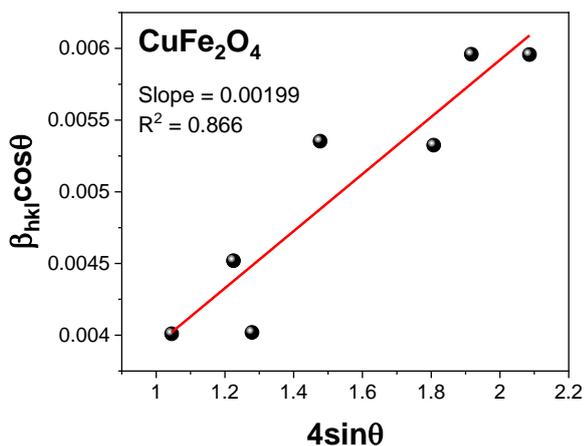
Fig. 3. Williamson-Hall plot for CuFe$_2$O$_4$ in the case of isotropic deformation.

2.1.3. Size-Strain Plot (SSP) Method

The Williamson-Hall method analyzes peak broadening in relation to the diffraction angle (2θ) and attributes it to both size and strain effects. However, alternative models focus on peak profile analysis. One such approach is the Size-Strain Plot (SSP) method [42], which interprets the X-ray diffraction (XRD) peak profile as a hybrid of Lorentzian and Gaussian functions. In this model, the broadening due to particle size is represented by a Lorentzian function, while the broadening caused by strain is depicted using a Gaussian function. This combination allows for a more comprehensive interpretation of the peak profile zone (PPZ) expansion.

$$\beta_{hkl} = \beta_L + \beta_G \qquad (9)$$

In this context, β_L and β_G represent peak broadening due to Lorentzian and Gaussian functions, respectively. The Size-Strain Plot (SSP) method often yields superior outcomes for isotropic broadening, particularly for low-angle reflections where the accuracy and precision exceed those observed at higher angles. At higher angles, the quality of X-ray diffraction (XRD) data tends to decrease, and peak overlap becomes more pronounced. Consequently, SSP calculations are performed using equation [43 38] as follows:

$$(d_{hkl}\beta_{hkl}cos\theta)^2 = \frac{k\lambda}{D}(d_{hkl}^2\beta_{hkl}^2 cos\theta) + \frac{\varepsilon^2}{4} \qquad (10)$$

Where d_{hkl} is the interplanar distance between (hkl) planes for a cubic crystal

$$d_{hkl}^2 = \frac{a^2}{h^2 + k^2 + l^2} \qquad (11)$$

Now, using equation (10), a graph is plotted where the term $(d_{hkl}^2\beta_{hkl}^2 cos\theta)$ is positioned on the X-axis and the value $(d_{hkl}\beta_{hkl}cos\theta)^2$ is placed on the Y-axis for each diffraction peak, as illustrated in Figure 4.

The slope of the line indicates an average particle size of 29.8 nm, and the y-intercept corresponds to the intrinsic strain in CuFe$_2$O$_4$ nanocrystals, measured $1{,}78 \cdot 10^{-3}$.
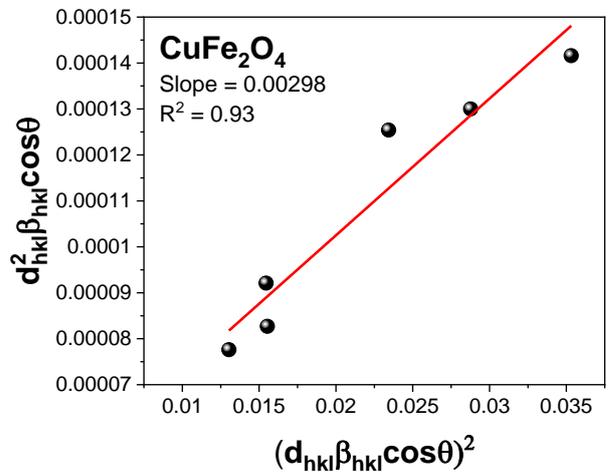
Fig. 4. Size-Strain Plot (SSP) analysis for CuFe$_2$O$_4$ sample.

2.1.4. Halder-Wagner method

In the SSP method, peak broadening due to particle

size is modeled as a Lorentzian function, and strain broadening as a Gaussian function. However, XRD peak profiles do not fit perfectly into either function type. The area under the XRD peak aligns well with the Gaussian function, but its rapid tail decay does not. Conversely, the tails of the peak profile match the Lorentzian function but do not correspond to the peak area as described in sources [43, 44]. To address this mismatch, the Halder-Wagner method is employed. This approach assumes that the peak broadening is a symmetric Voigt function, which is essentially a convolution of a Lorentzian and a Gaussian function, as noted in source [45]. By applying the Halder-Wagner method, the full width at half maximum (FWHM) of the physical profile for the Voigt function can be described in the following way:

$$\beta_{hkl}^2 = \beta_L \beta_{hkl} + \beta_G^2 \qquad (12)$$

Here, β_L and β_G represent the full width at half maximum (FWHM) of the Lorentzian and Gaussian functions, respectively. This method is particularly advantageous for analyzing peaks in the small to medium angle range, where there is minimal overlap between diffraction peaks. The Halder-Wagner method outlines the relationship between crystallite size and lattice strain as follows:

$$\left(\frac{\beta_{hkl}^*}{d_{hkl}^*}\right)^2 = \frac{1}{D}\frac{\beta_{hkl}^*}{d_{hkl}^{*2}} + \left(\frac{\varepsilon}{2}\right)^2 \qquad (13)$$

Where β_{hkl}^* is defined as $\beta_{hkl} \cdot cos\frac{\theta}{\lambda}$ and d_{hkl}^* is calculated as $2d_{hkl} \cdot sin\frac{\theta}{\lambda}$. The plot for equation (13) features $\frac{\beta_{hkl}^*}{(d_{hkl}^*)^2}$ on the X-axis and $\left(\frac{\beta_{hkl}^*}{d_{hkl}^*}\right)^2$ on the Y-axis for each peak in the X-ray pattern, as depicted in Figure 5.
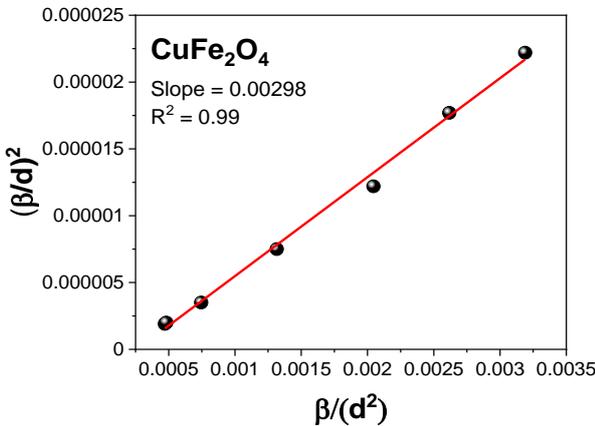
Fig. 5. Halder-Wagner plot for CuFe$_2$O$_4$.

The slope of the line in the graph indicates the average particle size, while the y-intercept reflects the intrinsic strain of CuFe$_2$O$_4$ nanocrystals. The plot calculates the average particle size as 29.8 nm, confirming the size estimates from the SSP model. Meanwhile, the strain value derived from the Halder-Wagner plot is $4.9 \cdot 10^{-3}$, approximately five times higher than those obtained using other models. This significant increase in the strain estimation can be attributed to the influence of data from

low- and medium-angle XRD peaks. Furthermore, the elevated strain values determined through the Halder-Wagner method might also be linked to crystal lattice dislocations [41], which are crucial in the broadening of reflection peaks at lower angles.

2.1.5. Modified Debye-Scherrer method

Sometimes, the modified Debye-Scherrer method is applied [46], where the logarithmic values of the broadening and the inverse of the reflex position are analyzed. Figure 6 illustrates this relationship for the synthesized sample.
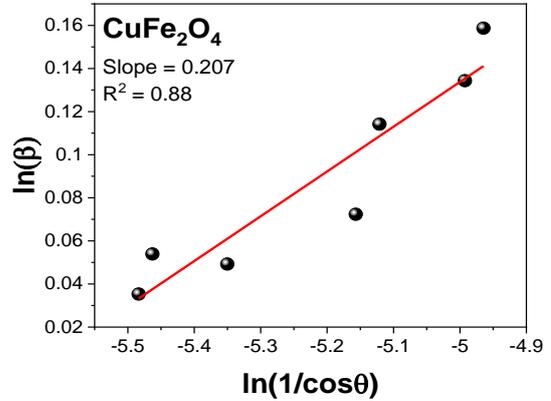
Fig. 6. Modified Debye-Scherrer plot for CuFe$_2$O$_4$.

The modified dependency produces the same relationships as depicted in Figure 2; however, the data points now align more closely with a straight line. Table 1 presents all the calculated values for average size and natural deformation, along with other elastic parameters.

This table demonstrates that the average sizes determined by the methods described above are proportional to each other.

2.2. Morphological analysis

Figure 7a displays the typical morphologies of CuFe$_2$O$_4$ particles as observed through scanning electron microscopy (SEM). The particles are nanosized and predominantly spherical in form. The distribution of CuFe$_2$O$_4$ particles, as determined from SEM, is presented in the histogram in Figure 7b. The analysis shows that the particles are significantly larger than the crystallite sizes measured through X-ray techniques. This discrepancy arises because the microparticles observed are actually aggregates of much smaller crystallites. Additionally, the tendency of these particles to cluster together is likely due to their magnetic properties [47]. However, some particles shown in the SEM images align with the sizes obtained from X-ray diffraction (XRD) data. The average particle size was calculated by fitting the particle size distribution histogram to a log-normal distribution function, as outlined in reference [48].

$$f(D) = \left(\frac{1}{\sqrt{2\pi}\sigma_D}\right)exp\left[-\frac{ln^2\left(\frac{D}{D_0}\right)}{2\sigma^2}\right] \qquad (14)$$

Parameters of CuFe₂O₄ nanoparticles, obtained by different models

	Sherrer Method	W-H Method		SSP Method		H-W Method		Modified D-Sherrer Method
	Size D (nm)	Size D (nm)	Strain ε (10⁻³)	Size D (nm)	Strain ε (10⁻³)	Size D (nm)	Strain ε (10⁻³)	Size D (nm)
CuFe₂O₄	28.0	28.4	1.99	29.8	1.78	29.8	4.94	28.8
errors	±0.1	±0.1	±0.01	±0.1	±0.01	±0.1	±0.01	±0.1
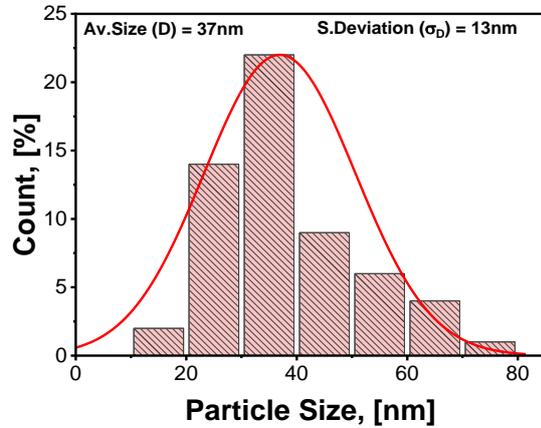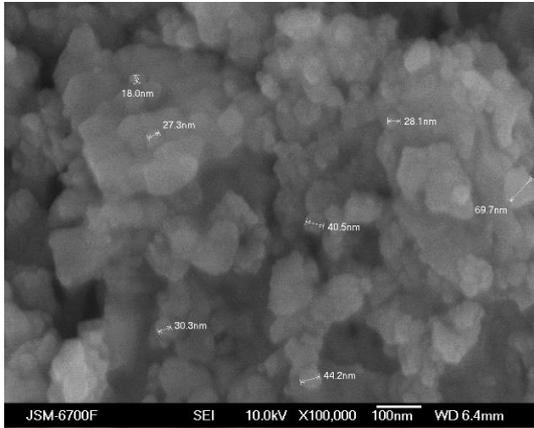
Fig. 7. (a) SEM image of the CuFe₂O₄ system obtained by sol-gel autocombustion; (b) Particle size distribution.

2.3. FTIR Analysis and Elastic Properties Calculation

Figure 8 illustrates the FTIR spectrum in the wavenumber range of 150–650 cm⁻¹ for the CuFe₂O₄ sample at room temperature.
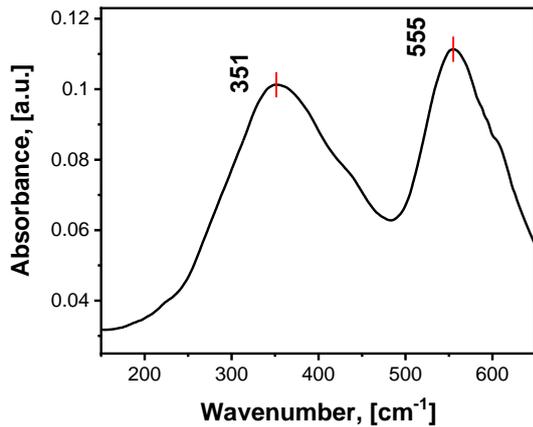
Fig. 8. FTIR spectrum in the wavenumber range of 150–650 cm⁻¹ for the CuFe₂O₄ sample.

From the FTIR spectra, two distinct absorption bands at 555 cm⁻¹ and 351 cm⁻¹ are observed. The symmetrical stretching vibrations of metal–oxygen at tetrahedral and octahedral sites have been observed at the higher band, and lower band, respectively.

2.3.1. Calculation of force constant.

The wavenumbers corresponding to the infrared active phonon modes are directly related to the force constants. The force constants, k_T and k_O, at the tetrahedral and octahedral sites of the cubic spinel structure, respectively, have been calculated using the Waldron

relation [49]:

$$k_T = 4\pi^2 c^2 v_1^2 \mu \qquad (15)$$

$$k_O = 4\pi^2 c^2 v_2^2 \mu \qquad (16)$$

$$k_{AV} = (k_T + k_O)/2 \qquad (17)$$

In this case, c represents the speed of light, and μ denotes the reduced mass, calculated using the equation:

$$\mu = \frac{m_1 \cdot m_2}{m_1 + m_2} \qquad (18)$$

where m1 is the weighted average of atomic weights of the cations residing at A-site or B-site, while m2 is the atomic weight of oxygen anion.

Here, m_1 is the weighted average of the atomic weights of the cations located at either the A-site or B-site, and m_2 refers to the atomic weight of the oxygen anion.

2.3.2 Elastic properties analysis.

Ferrites present significant elastic and thermal properties, which arise from their interatomic and interionic forces. Typically, the elastic characteristics of these materials are assessed through the application of external stress. However, according to various studies [50], a method that combines both structural and FTIR data has been developed to calculate these properties. This approach facilitates an examination of the relationships between elastic and thermal properties and other characteristics of the materials.

In materials with cubic symmetry, the stiffness constants C_{11}, C_{12}, and C_{44} are predominantly considered. Here, C_{11} corresponds to the elastic modulus in length, while C_{12} and C_{44} relate to the shape elasticity. The stiffness constants C_{11} and C_{12} are derived using equations (19-20), with the

resulting values presented in Table 2 [51].

$$C_{11} = \frac{k_{AV}}{a} \qquad (19)$$

$$C_{12} = \frac{\sigma C_{11}}{1-\sigma} \qquad (20)$$

Here, σ represents Poisson's ratio as a function of the pore fraction P:

$$\sigma = 0.324(1 - 1.043P) \qquad (21)$$

The bulk modulus (B), rigidity modulus (G), Young's modulus (E), Poisson's ratio (σ), longitudinal wave velocity (υ_L), transverse wave velocity (υ_T), and the mean velocity (υ_M) have been determined using the equations provided below:

$$B = \frac{1}{3}(C_{11} + 2C_{12}) \qquad (22)$$

$$\upsilon_L = \sqrt{\frac{C_{11}}{d_x}} \qquad (23)$$

Here d_X represents the X-ray density,

$$\upsilon_T = \frac{\upsilon_L}{\sqrt{3}} \qquad (24)$$

$$G = d_x \upsilon_t^2 \qquad (25)$$

$$E = 2(1 + \sigma)G \qquad (26)$$

$$\upsilon_M = \left(\frac{1}{3}\left(\frac{2}{\upsilon_T^3} + \frac{1}{\upsilon_L^3} \right) \right)^{-1/3} \qquad (27)$$

Calculated elastic properties along with force constants are given in the table below.

2.3.3 Thermodynamic properties.

The Debye temperature, θ_D, is an important parameter for understanding the thermodynamic properties of a solid [52], particularly because it is derived from the maximum lattice vibration frequencies of atoms within the material. This temperature provides insights into various physical properties such as specific heat and thermal conductivity at low temperatures. It can be calculated using Anderson's formula, as shown in the equation:

$$\theta_D = \frac{h}{2\pi k_B} \left(\frac{3q d_x N_A}{4\pi M} \right)^{\frac{1}{3}} \upsilon_M \qquad (28)$$

Thermal conductivity is another key thermodynamic property that measures a material's capacity to transfer heat. It is critical for applications where heat dissipation is essential, such as in thermal management systems for electronics. This value can be determined by the following equation:

$$K_{min} = k_B \upsilon_M \left(\frac{M}{q d_x N_A} \right)^{-2/3} \qquad (29)$$

It has been found that the Debye temperature for the material is 593 K, suggesting robust lattice vibrations at this temperature. Meanwhile, the calculated minimum thermal conductivity is 1.29 W/m·K, indicating the material's efficiency in heat transfer under specific conditions. These values not only provide insights into the material's vibrational and heat transfer characteristics but also help in predicting its behavior in various thermal environments, assisting in the design of applications where thermal management is critical.

2.4. Electron densities distribution maps

The electron density of the most intense plane, (311), is illustrated in Fig. 9 (a, b). The GFourier program from the FullProf package was used for electron density mapping to analyze the distribution within the unit cell. This analysis helps identify the atomic positions of the components within the unit cell. Electron density is calculated through the Fourier transform of the geometrical structural factor over the entire unit cell [53]. The scattering of electrons is depicted in both two-dimensional (2D) and three-dimensional (3D) Fourier

Table 2.

Calculated elastic parameters of CuFe$_2$O$_4$ sample

K_T	K_O	υ_L	υ_T	υ_{AV}	B	E	G	σ	υ_M	Θ'_D	Θ_D
N/m		m/s			GPa				m/s	K	
137.6	76.29	5550	3510	4530	127.78	169.97	61.43	0.38	936.89	133	213
±0.1	±0.01	±1	±1	±1	±0.01	±0.01	±0.01	±0.01	±0.01	±1	±1
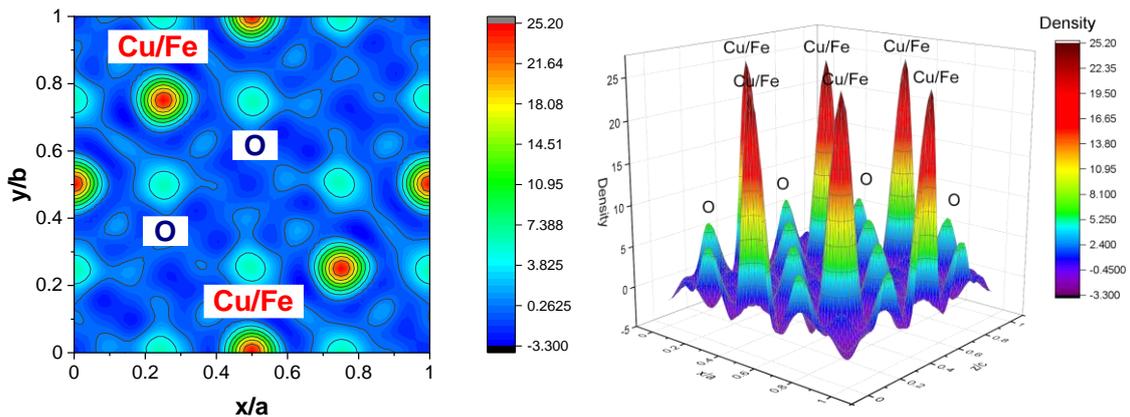
Fig. 9. (a) 2D electron density map in the unit cell of CuFe$_2$O$_4$ nanoparticles; (b) 3D electron density map in the unit cell of CuFe$_2$O$_4$ nanoparticles. (Note: Electron density is measured in electrons per cubic angstrom, e/Å³).

maps. Electron density is defined as a periodic function of position, peaking at the atomic sites and reaching a minimum in the spaces between atoms. In the displayed maps, high electron-density areas are colored orange, while low-density areas are shown in blue. To explain the chemical bonding and charge distribution in the $CuFe_2O_4$ compound, 2D-Fourier maps are typically represented as contours that illustrate the electron density distribution around each atom. Denser and thicker electron density contours indicate the presence of heavier elements within the unit cell.

The 3D-Fourier maps display a matrix, signifying a single level of electron density. Figure 3(a) showcases the typical two-dimensional Fourier electron density distribution for Cu/Fe and O atoms along the y_B plane (x = 0) within the unit cell. The thick, dense circular contours around Cu/Fe are likely due to the distribution of electrons in the valence d orbitals. Conversely, the contours around O atoms may relate to the electron distribution in valence 2s and 2p orbitals. In Fig. 3(a), the blue color represents the zero-level density contour, whereas the colored contours around the Cu/Fe and O atoms indicate varying electron density levels.

Figure 3(b) presents the 3D Fourier electron density maps for Cu, Fe, and O elements in the $CuFe_2O_4$ unit cell at x = 0. It highlights significant peaks at the 8a and 16d sites for Cu cations, with an intermediary peak correlating to similar sites for Fe cations. X-ray scattering is influenced by the electron count around an atom; Cu atoms, having more electrons than Fe, scatter X-rays more intensely, making the Cu-related peaks more prominent than those of Fe. Research utilizing the FullProf software to map electron densities in oxides has documented similar findings, as reported in recent literature [53-55].

Conclusions

The $CuFe_2O_4$ nanoparticles were synthesized using the sol-gel autocombustion method with citric acid as a fuel. Their crystallinity and phase composition were then characterized using X-ray diffraction. The broadening of the diffraction peaks was analyzed to determine the average particle size and calculate the microstresses within the crystals. This analysis used the Debye-Scherrer, Williamson-Hall, size-strain plot (SSP method), and Halder-Wagner methods.

The average particle size determined is between 28-29 nm, consistent across various measurement methods. Elastic microparameters calculated using the Williamson-Hall and SSP methods are similar, ranging from $0.9 \cdot 10^{-3}$ to $1.7 \cdot 10^{-3}$. The elastic properties derived from the Halder-Wagner method are approximately five times greater. This difference is due to the Halder-Wagner method's consideration of the contributions from low- and medium-angle reflections and its accounting for the presence of

dislocations within the crystal lattice. The crystallite sizes derived from SEM images are larger, averaging 37 nm, suggesting some degree of particle agglomeration due to their magnetic characteristics. Additionally, the elastic properties identified through FTIR analysis reflect the interatomic and interionic interactions within the particles.

The electron density map, derived from XRD data, revealed that the highest intensity is observed in the (311) direction. The most pronounced peaks are associated with Cu cations at the 8a and 16d sites, with additional intermediate peaks at these positions for iron cations. This pattern arises because iron has fewer electrons than copper, resulting in less intense peaks.

Mazurenko Julia – Candidate of Physical and Mathematical Sciences (Ph.D.), Docent, Associate Professor at the Department of Medical Informatics, Medical and Biological Physics;
Kaykan Larysa – Doctor of Physical and Mathematical Sciences, Senior Researcher at the Laboratory for Physics of Magnetic Films No 23;
Bandura Khrystyna – Candidate of Physical and Mathematical Sciences (Ph.D.), Assistant at the Department of Medical Informatics, Medical and Biological Physics;
Vyshnevskyi Oleksii – Candidate of Geological Sciences (PhD), Leading Researcher at the Department of Diamond;
Moiseienko Mykola – Doctor of Biological Sciences, Professor, Head of the Department of Medical Informatics, Medical and Biological Physic;
Kuzyshyn Myroslav – Candidate of Physical and Mathematical Sciences (Ph.D.), Assistant at the Department of Medical Informatics, Medical and Biological Physics;
Ostapovych Nataliia – Candidate of Pedagogical (Ph.D.), Docent, Associate at the Department of Medical Informatics, Medical and Biological Physics.

[1] H. K. Dubey, & P. Lahiri. *Synthesis, structural, dielectric and magnetic properties of Cd²⁺ based Mn nanosized ferrites,* Materials Technology (UK), 131–144, 36(3), (2021); https://doi.org/10.1080/10667857.2020.1734728.

[2] E. E. Ateia, M. K. Abdelmaksoud, M. M. Arman, & A. S. Shafaay. *Comparative study on the physical properties of rare-earth-substituted nano-sized CoFe₂O₄.* Applied Physics. A, Materials Science & Processing, 126(2), (2020); https://doi.org/10.1007/s00339-020-3282-5.

[3] S. A. Mazen, H. M. Elsayed, & N. I. Abu-Elsaad. *A comparative study of different concentrations of (Co/Ni/Cu) effects on elastic properties of Li–Mn ferrite employing IR spectroscopy and ultrasonic measurement*. Ceramics International, 26635–26642, 47(19), (2021); https://doi.org/10.1016/j.ceramint.2021.06.071.

[4] J. B. Shitole, S. N. Keshatti, S. M. Rathod, & S. S. Jadhav. *Y3+ composition and particle size influenced magnetic and dielectric properties of nanocrystalline $Ni_{0.5}Cu_{0.5}Y_xFe_{2-x}O_4$ ferrites*. Ceramics International, 17993–18002, 47(13), (2021); https://doi.org/10.1016/j.ceramint.2021.03.114.

[5] J. Mazurenko, L. Kaykan, A. K. Sijo, M. Moiseienko, M. Kuzyshyn, N. Ostapovych, & M. Moklyak. *The influence of reaction medium pH on the structure, optical, and mechanical properties of nanosized Cu-Fe ferrite synthesized by the sol-gel autocombustion method*. Journal of Nano Research, 65–84, 81, (2023); https://doi.org/10.4028/p-d2fqah.

[6] T. Dippong, D. Toloman, M. Dan, E. A. Levei, & O. Cadar. *Structural, morphological and photocatalytic properties of Ni-Mn ferrites: Influence of the Ni:Mn ratio*. Journal of Alloys and Compounds, 913, 165129, (2022); https://doi.org/10.1016/j.jallcom.2022.165129.

[7] R. Singh Yadav, I. Kuřitka, J. Vilcakova, T. Jamatia, M. Machovsky, D. Skoda, P. Urbánek, M. Masař, M. Urbánek, L. Kalina, & J. Havlica. *Impact of sonochemical synthesis condition on the structural and physical properties of MnFe2O4 spinel ferrite nanoparticles*. Ultrasonics Sonochemistry, 61, 104839, (2020); https://doi.org/10.1016/j.ultsonch.2019.104839.

[8] R. Zapukhlyak, M. Hodlevsky, V. Boychuk, J. Mazurenko, V. Kotsyubynsky, L. Turovska, B. Rachiy, & S. Fedorchenko. *Structure and magnetic properties of hydrothermally synthesized $CuFe_2O_4$ and $CuFe_2O_4/rGO$ composites*. Journal of Magnetism and Magnetic Materials, 587 171208 (2023); https://doi.org/10.1016/j.jmmm.2023.171208.

[9] R. Qindeel N. H. Alonizan E. A. Alghamdi & M. A. Awad. *Synthesis and characterization of spinel ferrites for microwave devices*. Journal of Sol-Gel Science and Technology, 593–599, 97(3), (2021); https://doi.org/10.1007/s10971-021-05470-9.

[10] Y. J. Xu, S. Y. Song, C. X. Li, B. Hong, & X. Q. Wang. *Magnetic behavior, photocatalytic activity and gas-sensing performance of porous lanthanum ferrites powders*. Materials Chemistry and Physics, 267, 124628, (2021); https://doi.org/10.1016/j.matchemphys.2021.124628.

[11] M. J. Sadiq Mohamed, S. Caliskan, M. A. Gondal, M. A. Almessiere, A. Baykal, & A. Roy. *Se-doped magnetic co–Ni spinel ferrite nanoparticles as electrochemical catalysts for hydrogen evolution*. ACS Applied Nano Materials, 7330–7341, 6(9), (2023); https://doi.org/10.1021/acsanm.3c00464.

[12] N. K. Gupta, Y. Ghaffari, S. Kim, J. Bae, K. S. Kim, & M. Saifuddin. *Photocatalytic degradation of organic pollutants over MFe_2O_4 (M = Co, Ni, Cu, Zn) nanoparticles at neutral pH*. Scientific Reports, 10(1), (2020); https://doi.org/10.1038/s41598-020-61930-2.

[13] B. Shi, Y. Wang, I. Ahmed, & B. Zhang. *Catalytic degradation of refractory phenol sulfonic acid by facile, calcination-free cobalt ferrite nanoparticles*. Journal of Environmental Chemical Engineering, 107616, 10(3), (2022); https://doi.org/10.1016/j.jece.2022.107616.

[14] A. Becker, K. Kirchberg, & R. Marschall. *Magnesium ferrite ($MgFe_2O_4$) nanoparticles for photocatalytic antibiotics degradation*. Zeitschrift Für Physikalische Chemie (Frankfurt Am Main, Germany), 645–654, 234(4), (2020); https://doi.org/10.1515/zpch-2019-1430.

[15] K. K. Kefeni, T. A. M. Msagati, T. T. I. Nkambule, & B. B. Mamba. *Spinel ferrite nanoparticles and nanocomposites for biomedical applications and their toxicity*. Materials Science & Engineering. C, Materials for Biological Applications, 110314, 107, (2020); https://doi.org/10.1016/j.msec.2019.110314.

[16] J. Muhamad Arshad, W. Raza, N. Amin, K. Nadeem, M. Imran Arshad, & M. Azhar Khan. *Synthesis and characterization of cobalt ferrites as MRI contrast agent*. Materials Today: Proceedings, S50–S54, 47, (2021); https://doi.org/10.1016/j.matpr.2020.04.746 .

[17] M. I. A. Abdel Maksoud, M. M. Ghobashy, A. S. Kodous, & A. H. Ashour. *Insights on magnetic spinel ferrites for targeted drug delivery and hyperthermia applications*. Nanotechnology Reviews, 372–413, 11(1), (2022); https://doi.org/10.1515/ntrev-2022-0027.

[18] G. Nandhini, & M. K. Shobana. *Role of ferrite nanoparticles in hyperthermia applications*. Journal of Magnetism and Magnetic Materials, 552, 169236, (2022); https://doi.org/10.1016/j.jmmm.2022.169236.

[19] D. O. Morais, A. Pancotti, G. S. de Souza, & J. Wang. *Synthesis, characterization, and evaluation of antibacterial activity of transition metal oxyde nanoparticles*. Journal of Materials Science. Materials in Medicine, 32(9), (2021); https://doi.org/10.1007/s10856-021-06578-8.

[20] C. Joseph Prabagar, S. Anand, M. Asisi Janifer, S. Pauline, & P. A. S. Theoder. *Effect of metal substitution (Zn, Cu and Ag) in cobalt ferrite nanocrystallites for antibacterial activities*. Materials Today: Proceedings, 1999–2006, 47, (2021); https://doi.org/10.1016/j.matpr.2021.04.150.

[21] V. K. Surashe, V. Mahale, A. P. Keche, & R. G. Dorik. *Structural and electrical properties of copper ferrite ($CuFe_2O_4$) NPs*. Journal of Physics. Conference Series, 1644(1), 012025, (2020); https://doi.org/10.1088/1742-6596/1644/1/012025 .

[22] F. H. Mulud, N. A. Dahham, & I. F. Waheed. *Synthesis and characterization of copper ferrite nanoparticles*. IOP Conference Series. Materials Science and Engineering, 072125, 928(7), (2020); https://doi.org/10.1088/1757-899x/928/7/072125.

[23] K. Cui, M. Sun, J. Zhang, J. Xu, & Yuan, C. *Facile solid-state synthesis of tetragonal CuFe₂O₄ spinels with improved infrared radiation performance.* Ceramics International, 10555–10561, 48(8), (2022); https://doi.org/10.1016/j.ceramint.2021.12.268.

[24] S. Mallesh, M. Gu, & K. H. Kim. *Cubic to tetragonal phase transition in CuFe₂O₄.* Experimental details nanoparticles. Journal of Magnetics, 7–13, 26(1), (2021); https://doi.org/10.4283/jmag.2021.26.1.007.

[25] R., Dhyani, R. C., Srivastava, & G. Dixit. *Study of magnetic and temperature-dependent dielectric properties of Co-CuFe₂O₄ nanoferrites.* Journal of Electronic Materials, 5492–5507, 51(10), (2022); https://doi.org/10.1007/s11664-022-09831-0.

[26] L. Kaykan, A. Sijo, J. Mazurenko, & A. Żywczak. *Influence of the preparation method and aluminum ion substitution on the structure and electrical properties of lithium–iron ferrites.* Applied Nanoscience, 503–511, 12(3), (2022); https://doi.org/10.1007/s13204-021-01691-0

[27] S. K. Sen, T. C. Paul, S. Dutta, M. N. Hossain, & M. N. H. Mia. *XRD peak profile and optical properties analysis of Ag-doped h-MoO₃ nanorods synthesized via hydrothermal method.* Journal of Materials Science: Materials in Electronics, 1768–1786, 31(2), (2020); https://doi.org/10.1007/s10854-019-02694-y.

[28] T. Ungár. *Microstructural parameters from X-ray diffraction peak broadening.* Scripta Materialia, 777–781, 51(8), (2004); https://doi.org/10.1016/j.scriptamat.2004.05.007.

[29] W. H. Hall. *X-ray line broadening in metals.* Proceedings of the Physical Society, 741–743, 62(11), (1949); https://doi.org/10.1088/0370-1298/62/11/110.

[30] B. E. Warren, & B. L. Averbach. *The separation of cold-work distortion and particle size broadening in X-ray patterns.* Journal of Applied Physics, 497–497, 23(4), (1952); https://doi.org/10.1063/1.1702234.

[31] D. Balzar, & H. Ledbetter. *Voigt-function modeling in Fourier analysis of size- and strain-broadened X-ray diffraction peaks.* Journal of Applied Crystallography, 97–103, 26(1), (1993); https://doi.org/10.1107/s0021889892008987.

[32] L. Kaykan, J. Mazurenko, N. Ostapovych, A. Sijo, N. 'Ivanichok. *Effect of pH on structural morphology and magnetic properties of ordered phase of cobalt doped lithium ferrite nanoparticles synthesized by sol-gel auto-combustion method.* Journal of Nano- and Electronic Physics, 12(4), (2020); https://doi.org/10.21272/jnep.12(4).04008.

[33] L. Kaykan, J. Mazurenko, I. Yaremiy, K. Bandura, N. Ostapovych. *Effect of nickel ions substitution on the structural and electrical properties of a nanosized lithium-iron ferrite obtained by the sol-gel auto-combustion method.* Journal of Nano- and Electronic Physics, 11(5), (2019); https://doi.org/10.21272/jnep.11(5).05041.

[34] N. Khan, I. Irshad, B. S. Almutairi, A. Dahshan, A. Husssain, & M. Sagir. *Sol-gel auto-combustion synthesis and characterization of Nd3+ doped Cu₀.₅Co₀.₅Fe₂₋ₓNdₓO₄ (x = 0.0, 0.1, 0.2, 0.3, 0.4, & 0.5) spinel ferrites.* Ceramics International, 8594–8601, 50(6), (2024); https://doi.org/10.1016/j.ceramint.2023.08.037.

[35] E.H. Nickel. *The new mineral cuprospinel (CuFe₂O₄) and other spinels from an oxidized ore dump at Baie Verte, Newfoundland.* Canadian Mineralogist: 11, 1003-1007, (1973).

[36] K. Momma, & F. Izumi. *VESTA 3for three-dimensional visualization of crystal, volumetric and morphology data.* Journal of Applied Crystallography, 1272–1276, 44(6), (2011); https://doi.org/10.1107/s0021889811038970.

[37] K. Pubby, S. S. Meena, S. M. Yusuf, & S. Bindra Narang. *Cobalt substituted nickel ferrites via Pechini's sol–gel citrate route: X-band electromagnetic characterization.* Journal of Magnetism and Magnetic Materials, 430–445, 466, (2018); https://doi.org/10.1016/j.jmmm.2018.07.038.

[38] S. B. Waje, M. Hashim, W. D. W. Yusoff, & Z. Abbas. *X-ray diffraction studies on crystallite size evolution of CoFe₂O₄ nanoparticles prepared using mechanical alloying and sintering.* Applied Surface Science, 3122–3127, 256(10), (2010); https://doi.org/10.1016/j.apsusc.2009.11.084.

[39] R. S. Shitole, V. K. Barote, S. B. Kadam, & R. H. Kadam. *Williamson-Hall strain analysis, cation distribution and magnetic interactions in Dy³⁺ substituted zinc-chromium ferrite.* Journal of Magnetism and Magnetic Materials, 588, 171468, (2023); https://doi.org/10.1016/j.jmmm.2023.171468.

[40] A. M. Nashaat, A. Abu El-Fadl, M. A. Kassem, & H. Nakamura. *Optimizing a microwave-combustion synthesis and particle-size dependent magnetic properties of M-type Sr ferrite.* Materials Chemistry and Physics, 305, 128008, (2023); https://doi.org/10.1016/j.matchemphys.2023.128008.

[41] S. Debnath, K. Deb, B. Saha, & R. Das. *X-ray diffraction analysis for the determination of elastic properties of zinc-doped manganese spinel ferrite nanocrystals (Mn₀.₇₅Zn₀.₂₅Fe₂O₄), along with the determination of ionic radii, bond lengths, and hopping lengths.* The Journal of Physics and Chemistry of Solids, 105–114, 134, (2019); https://doi.org/10.1016/j.jpcs.2019.05.047.

[42] S. Debnath, & R. Das. *Cobalt doping on nickel ferrite nanocrystals enhances the micro-structural and magnetic properties: Shows a correlation between them.* Journal of Alloys and Compounds, 852, (2021); https://doi.org/10.1016/j.jallcom.2020.156884.

[43] G. S. Thool, A. K. Singh, R. S. Singh, A. Gupta, & M. A. B. H. Susan. *Facile synthesis of flat crystal ZnO thin films by solution growth method: A micro-structural investigation.* Journal of Saudi Chemical Society, 712–721, 18(5), (2014);https://doi.org/10.1016/j.jscs.2014.02.005.

[44] S. E. M. Ghahfarokhi, M. Ahmadi, & I. Kazeminezhad. *Effects of Bi³⁺ substitution on structural, morphological, and magnetic properties of cobalt ferrite nanoparticles.* Journal of Superconductivity and Novel Magnetism, 32(10), 3251–3263, (2019); https://doi.org/10.1007/s10948-019-5058-8.

[45] U. Kumar, D. Padalia, P. Kumar, & P. Bhandari. *Estimation of lattice strain and structural study of BaTiO₃/PS polymer composite using X-ray peak profile analysis.* Journal of Nanoparticle Research: An Interdisciplinary Forum for Nanoscale Science and Technology, 25(6), (2023); https://doi.org/10.1007/s11051-023-05779-2.

[46] K. Mabhouti, P. Norouzzadeh, & M. Taleb-Abbasi. *Effects of Fe, Co, or Ni substitution for Mn on La₀.₇Sr₀.₃MnO₃ perovskite: Structural, morphological, and optical analyses.* Journal of Non-Crystalline Solids, 610, (2023); https://doi.org/10.1016/j.jnoncrysol.2023.122283.

[47] Kumar S. Ravina, S. Z. Hashmi, G. Srivastava, J. Singh, A. M. Quraishi, & P. A. Alvi. *Synthesis and investigations of structural, surface morphology, electrochemical, and electrical properties of NiFe₂O₄ nanoparticles for usage in supercapacitors.* Journal of Materials Science: Materials in Electronics, 34(10), (2023); https://doi.org/10.1007/s10854-023-10312-1.

[48] P. Acharya, R. Desai, V. K. Aswal, & R. V. Upadhyay. *Structure of Co-Zn ferrite ferrofluid: A small angle neutron scattering analysis.* Pramana, 1069–1074, 71(5), (2008); https://doi.org/10.1007/s12043-008-0225-7

[49] R. D. Waldron. *Infrared spectra of ferrites.* The Physical Review, 1727–1735, 99(6), (1955); https://doi.org/10.1103/physrev.99.1727.

[50] V. G. Patil, S. E. Shirsath, S. D. More, S. J. Shukla, & K. M. Jadhav. *Effect of zinc substitution on structural and elastic properties of cobalt ferrite.* Journal of Alloys and Compounds, 199–203, 488(1), (2009); https://doi.org/10.1016/j.jallcom.2009.08.078.

[51] S. M. Patange, S. E. Shirsath, S. P. Jadhav, V. S. Hogade, S. R. Kamble & K. M. Jadhav. *Elastic properties of nanocrystalline aluminum substituted nickel ferrites prepared by co-precipitation method.* Journal of Molecular Structure, 40–44, 1038, (2013); https://doi.org/10.1016/j.molstruc.2012.12.053.

[52] M. R. Patil, M. K. Rendale, S. N. Mathad, & R. B. Pujar. *FTIR spectra and elastic properties of Cd-substituted Ni–Zn ferrites.* International Journal of Self-Propagating High-Temperature Synthesis, 33–39, 26(1), (2017); https://doi.org/10.3103/s1061386217010083.

[53] M. Thavarani, M. C. Robert, N. Pavithra, R. Saravanan, Y. B. Kannan, & S. B. Prasath. *Effect of Ca²⁺ doping on the electronic charge density and magnetic properties of ZnFe₂O₄ spinel ferrites.* Journal of Materials Science: Materials in Electronics, 4116–4131, 33(7), (2022); https://doi.org/10.1007/s10854-021-07605-8.

[54] N. Abinaya, M. C. Robert, N. Srinivasan, & S. Saravanakumar. *Electron density mapping and bonding in Mn doped CoFe₂O₄ using XRD, and its correlation with room temperature optical and magnetic properties.* Journal of Magnetism and Magnetic Materials, 170938, 580, (2023); https://doi.org/10.1016/j.jmmm.2023.170938.

[55] S. K. Ahmed, M. F. Mahmood, M. Arifuzzaman, & M. Belal Hossen. *Enhancement of electrical and magnetic properties of Al³⁺ substituted CuZn nano ferrites with structural Rietveld refinement.* Results in Physics, 104833, 30, (2021); https://doi.org/10.1016/j.rinp.2021.104833.

Ю. Мазуренко[1,2], Л. Кайкан[4], Х. Бандура[1], О. Вишневський[4] М. Мойсеєнко[1], М. Кузишин[1], Н. Остапович[1]

Встановлення структурно-морфологічних і пружних властивостей нанорозмірної шпінелі CuFe₂O₄, отриманої методом золь-гель автоспалювання

[1]Івано-Франківський національний медичний університет, м. Івано-Франківськ, Україна; yumazurenko@ifnmu.edu.ua
[2]Faculty of Physics and Applied Computer Science, AGH University of Krakow, Krakow, Poland.
[3]Інститут металофізики ім. Г. В. Курдюмова НАН України, Київ, Україна. larysa.kaykan@gmail.com
[4]Інститут геохімії, мінералогії та рудоутворення імені М.П. Семененка НАН України, Київ, Україна, vyshnevskyy@i.ua

Нанорозмірний ферит CuFe₂O₄ був синтезований за допомогою методу золь-гель автоспалювання, використовуючи нітрати заліза та міді та лимонну кислоту в якості палива. Після синтезу ферит аналізували за допомогою рентгенівської дифракції (XRD), інфрачервоної спектроскопії з перетворенням Фур'є (FTIR) та скануючої електронної мікроскопії (SEM). Рентгенівські дослідження підтвердили кристалічність CuFe₂O₄, визначивши його як матеріал зі структурою змішаної шпінелі, що належить просторовій групі Fd3m. Виміри розмірів частинок, проведені методами Дебая-Шеррера, Вільямсона-Холла, Гальдера-Вагнера, модифікованого Дебая-Шеррера та діаграмою напруги-деформації (SSP), показали узгоджену середню величину близько 28,3 нм. Пружні характеристики наночастинок були детально охарактеризовані, включаючи використання розширення дифракційних ліній (методом Вільямсона-Холла) та FTIR-спектроскопії для оцінки структурних властивостей матеріалів. Окрім того, було визначено мікродеформації у кристалічній гратці та обчислено такі пружні константи, як модуль Юнга, модуль зсуву, температура Дебая та швидкості розповсюдження хвиль. Також було побудовано розподіл електронної густини згідно з даними рентгенівської дифракції.

Ключові слова: наноструктурні матеріали; мідний ферит; золь-гель автоспалювання; рентгенівська дифракція; мікроструктурний аналіз; метод Гальдера-Вагнера; скануюча електронна мікроскопія.